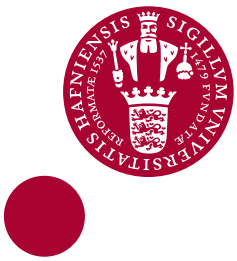

Imaging of dynamic magnetic fields with spin-polarized neutron beams

Tremsin, A. S.; Kardjilov, N.; Strobl, M.; Manke, I.; Dawson, M.; McPhate, J. B.; Vallerga, J. V.; Siegmund, O. H. W.; Feller, W. B.

Published in:
New Journal of Physics

DOI:
10.1088/1367-2630/17/4/043047

Publication date:
2015

Document version
Publisher's PDF, also known as Version of record

Imaging of dynamic magnetic fields with spin-polarized neutron beams

2015 New J. Phys. 17 043047

(http://iopscience.iop.org/1367-2630/17/4/043047)

New Journal of Physics
The open access journal at the forefront of physics

Deutsche Physikalische Gesellschaft DPG
IOP Institute of Physics

Published in partnership with: Deutsche Physikalische Gesellschaft and the Institute of Physics

OPEN ACCESS

RECEIVED
5 November 2014

ACCEPTED FOR PUBLICATION
17 March 2015

PUBLISHED
22 April 2015

PAPER

Imaging of dynamic magnetic fields with spin-polarized neutron beams

A S Tremsin[1], N Kardjilov[2], M Strobl[3,4], I Manke[2], M Dawson[2,6], J B McPhate[1], J V Vallerga[1], O H W Siegmund[1] and W B Feller[5]

[1] Space Sciences Laboratory, University of California at Berkeley, Berkeley, CA 94720, USA
[2] Helmholtz-Zentrum Berlin, D-14109 Berlin, Germany
[3] European Spallation Source (ESS) AB, SE-22100 Lund, Sweden
[4] Niels Bohr Institute, University of Copenhagen, Copenhagen, Denmark
[5] Nova Scientific, Inc. 10 Picker Rd., Sturbridge, MA 01566, USA
[6] Current address: University of Salford, Salford, M54WT, UK.

E-mail: ast@ssl.berkeley.edu

Keywords: neutron imaging, magnetic fields, non-destructive testing

Supplementary material for this article is available online

Abstract

Precession of neutron spin in a magnetic field can be used for mapping of a magnetic field distribution, as demonstrated previously for static magnetic fields at neutron beamline facilities. The fringing in the observed neutron images depends on both the magnetic field strength and the neutron energy. In this paper we demonstrate the feasibility of imaging periodic dynamic magnetic fields using a spin-polarized cold neutron beam. Our position-sensitive neutron counting detector, providing with high precision both the arrival time and position for each detected neutron, enables simultaneous imaging of multiple phases of a periodic dynamic process with microsecond timing resolution. The magnetic fields produced by 5- and 15-loop solenoid coils of 1 cm diameter, are imaged in our experiments with ~100 μm resolution for both dc and 3 kHz ac currents. Our measurements agree well with theoretical predictions of fringe patterns formed by neutron spin precession. We also discuss the wavelength dependence and magnetic field quantification options using a pulsed neutron beamline. The ability to remotely map dynamic magnetic fields combined with the unique capability of neutrons to penetrate various materials (e.g., metals), enables studies of fast periodically changing magnetic processes, such as formation of magnetic domains within metals due to the presence of ac magnetic fields.

1. Introduction

The unique ability of neutrons to penetrate materials opaque to other types of radiation, combined with their ability to interact with a magnetic field through the neutron spin precession, makes neutrons an excellent probe for remotely studying magnetic field distributions, even internally within solid objects. Various techniques utilizing polarized neutrons have been developed for the spatially resolved investigation of magnetic fields [1–14]. One of these techniques correlates the variation of neutron intensity with the magnetic field strength and direction, allowing effective magnetic field imaging [2, 3, 5–10]. Also interferometric and diffraction methods have been available for a number of years, where the dependence of the real part of the refractive index on the magnetic field strength can be exploited [1, 4, 11, 12] including methods utilizing spin echo [13, 14]. However the latter techniques operate with neutron beams of low intensity caused by all the necessary beam conditioning, and further, some of them require spatial scanning through the sample, and therefore provide very limited imaging statistics, but with the tradeoff of providing very good spatial resolution. The alternative approach combines the conventional neutron imaging technique (whereby the two-dimensional neutron flux intensity distribution is measured after the sample) with the neutron spin analysis [5–10]. Magnetic fields within relatively large areas (tens of centimeters in linear dimension) can be studied by this technique without spatial

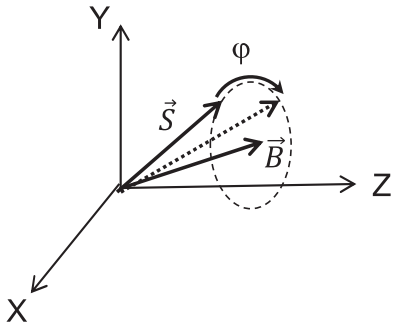

Figure 1. Precession of neutron spin vector $\vec{S}$ around the $\vec{B}$ vector of magnetic field.

scanning. Here the precession of the neutron spin in the presence of a magnetic field can be measured as a modulation of the intensity. Compared to a conventional neutron radiographic setup a spin polarizer/spin analyzer pair needs to be added, enabling studies of magnetic fields in combination with conventional absorption contrast imaging as well as other modalities such as neutron transmission tomography and Bragg edge imaging. Previous magnetic field studies concentrated on the imaging of static magnetic fields [5–10]. In this paper we demonstrate how similar methods can be implemented for studies of dynamic magnetic fields. However, the limited neutron flux available even at the present state-of-the-art neutron imaging facilities [15–20] necessarily limits these dynamic studies to either slowly changing magnetic fields (<1 Hz) or to periodic or cyclical processes where measurements of multiple cycles can be performed, in order to acquire sufficient neutron statistics for adequate imaging. Importantly however, the frequency of the periodic field can be as high as ~100 kHz, as the timing resolution of present neutron imaging detectors is in a sub-microsecond range [21]. This represents a significant advance in capability, compared with previous instrumentation.

In the presence of a magnetic field with non-zero component perpendicular to the neutron spin vector the spin undergoes precession around the magnetic field vector. That precession is described by the spin wave equation of an individual neutron spin $\vec{S}(t)$ propagating in a magnetic field $\vec{B}(t)$ [5, 8]

$$\frac{\mathrm{d}}{\mathrm{d}t}\vec{S}(t) = \gamma\left[\vec{S}(t) \times \vec{B}(t)\right], \tag{1}$$

where γ is the gyromagnetic ratio of the neutron ($-1.8\,324 \times 10^8$ rad s^{-1} T^{-1}). Thus the neutron spin precesses around the vector $\vec{B}(t)$ and has the instantaneous angular velocity $\omega(t) = \gamma\left|\vec{B}(t)\right| \sin\alpha$, where the angle α is the angle between the vectors $\vec{S}(t)$ and $\vec{B}(t)$, figure 1. The angle of rotation of spin component perpendicular to the magnetic field around the vector $\vec{B}(t)$ can be found then from the equation:

$$\mathrm{d}\varphi(t) = \omega(t)\,\mathrm{d}t. \tag{2}$$

Substituting the time variable t to the neutron path variable l ($t = l/v$) equation (2) becomes

$$\mathrm{d}\varphi(l) = \omega\frac{\mathrm{d}l}{v} = \frac{\omega\lambda m}{h}\mathrm{d}l = \frac{\gamma\lambda m}{h}\left|\vec{B}(l)\right|\sin\alpha\mathrm{d}l, \tag{3}$$

where v and λ are the neutron velocity and wavelength, respectively, m is the mass of neutron, h is the Plank constant and dl is a short section of neutron path l. Integrating equation (3) over the neutron path it is possible to calculate the angle of spin precession around the vector $\vec{B}(l)$:

$$\varphi = \frac{\gamma\lambda m}{h}\int\left|\vec{B}(l)\right|\sin\alpha\mathrm{d}l\,. \tag{4}$$

From equation (4) it is clear that the spin precession depends on the value and direction of the magnetic field and the neutron wavelength: for the same magnetic field the precession angle is larger for shorter wavelength neutrons. Therefore, to accurately probe the magnetic field by neutron spin precession at a continuous neutron source, a monochromatic beam of neutrons is required. At the same time, a polychromatic neutron beam can be used if the energy of each neutron is detected and therefore its wavelength λ is known, allowing for the reconstruction of value $\left|\vec{B}(l)\right|\sin\alpha$. The full three-dimensional reconstruction of the magnetic field vector $\vec{B}(l)$ requires multiple measurements with all possible combinations of the polarization vectors of incident neutron beam and the polarization analyzer, as explained in [6] and in section 1.1 below.

Let's consider a simple case, when neutrons propagate along the Z-axis and the magnetic field is directed along the same axis: $\vec{B}(l) = (B_x, B_y, B_z) = (0,\ 0,\ B_z)$. In that case the neutron spin always precesses around

the Z-axis and the angle of precession $\varphi = \frac{\gamma\lambda m}{h} B_z \Delta z$ is proportional to the value of the magnetic field and the neutron wavelength. Therefore the value of the magnetic field can be recovered if the angle φ is measured and the two-dimensional map of magnetic field values $B_z(x, y)$ can be found from the map of angles $\varphi(x, y)$. In our imaging experiments at a continuous neutron source we measured rather $\sin\varphi(x, y)$ than the angle φ. Therefore we measure the magnetic field accurate only with respect to an unknown offset (due to $\sin\varphi = \sin(\varphi + 2n\pi)$. The reconstruction of the absolute value of the magnetic field $B_z(x, y)$ requires *a priori* knowledge of the absolute value of the magnetic field at least in one point (e.g. the zero value of the field at a certain position x, y) or multiple measurements at different wavelengths [5, 24]. In the general case, when the magnetic field is not aligned with the Z-axis, the precession of the vector $\vec{S}(l)$ around the particular magnetic field vector $\vec{B}(l)$ at a point l along the neutron path can be calculated for a small increment dl. That process repeated for the entire path of the neutron travel between the polarizer and the analyzer can be used to correlate the measured spin precession angle with the magnetic field vector and thus be used for the reconstruction of the magnetic field. Note, however, that a discrete numerical calculation requires very small time steps and pixel sizes in the adiabatic case when the neutron spin projection on the vector B remains constant, i.e. the component of the neutron polarization parallel to the field follows directional changes of the magnetic field adiabatically.

1.1. Reconstruction of the magnetic field distribution from spin polarized neutron radiography

Disregarding neutron scattering and refraction (which only involves a small fraction of neutrons and very small beam deviations in most imaging experiments) it is assumed in our analysis that neutrons propagate along the Z-axis. If the incident neutron beam is spin- polarized and a polarization analyzer is installed between the sample and the detector, the intensity of the neutron flux $I(x, y)$ at position (x, y) behind the spin analyzer, is determined by the sample attenuation $\exp\left(-\int\sum(l)\,\mathrm{d}l\right)$, and the transmission function of the analyzer $\frac{1}{2}[1 + \cos\varphi(x, y)]$ [5–10]

$$I(x, y) = I_0(x, y)\exp\left(-\int\sum(x, y, z)\,\mathrm{d}z\right)\frac{1}{2}[1 + \cos\varphi(x, y)], \tag{5}$$

where $\Sigma(x, y, z)$ is the linear attenuation coefficient of the sample at position (x, y, z), $I_0(x, y)$ is the intensity of the incident beam, and φ is the angle between the neutron spin at the analyzer position and the analyzer maximum transmission direction. For experiments in which the magnetic field components perpendicular to the initial spin orientation are both zero (the angle φ is always equal to 0 as no spin precession is present for $\alpha = 0$) the measured intensity is determined only by the sample attenuation, as seen from the equation (5). Therefore if the magnetic field of the sample can be switched off (e.g. experiments with the magnetic field produced by a current) the influence of the sample attenuation can be measured first and used later for normalization to isolate only the magnetic field component from the equation (5). Another possibility is to switch the direction of polarizer by 180° and perform the measurements with spin up and spin down. From the measurement of spin up and down for both sample and open beam the degree of beam depolarization can be reconstructed accurately [8] and the attenuation due to the sample can be separated. As soon as at least one of the perpendicular field components is larger than 0 the neutron spin precesses and arrives at the analyzer with certain angle $\varphi(x, y)$ and therefore the measured intensity at that position is reduced by a factor of $\frac{1}{2}[1 + \cos\varphi(x, y)]$. Thus both perpendicular components of the magnetic field are probed in the experiment with a spin-polarized incident beam. Realignment of the spin polarizer and the analyzer along the other axes allows studies of the other pairs of the magnetic field components. In order to reconstruct the full three-dimensional distribution of the magnetic field (not intended in the present study) a set of nine measurements can be acquired with the polarizer P and analyzer A oriented along X or Y or Z axis in pairs as P_xA_x, P_yA_y, P_zA_z, P_xA_y, P_xA_z, P_yA_x, P_yA_z, P_zA_x, P_zA_y. In practice, instead of realignment of polarizer and analyzer it is easier to use a pair of spin flippers installed after the polarizer and before the analyzer [6].

2. Experimental setup

Our imaging experiments are conducted at the cold neutron beamline facility CONRAD [15] at the Helmholtz-Zentrum Berlin (HZB) providing a continuous flux of neutrons with the spectrum shown in figure 2. A spin polarizer with a magnetic field directed along the Y-axis was installed at the exit of cold neutron guide. The sample was placed in front of a spin-analyzer followed by a position sensitive detector, figure 3. Both the polarizer and the analyzer were bending-type spin polarization devices [25, 26], which transmit only neutrons with a particular spin state (parallel to its own magnetization axis) and absorbs neutrons with the other spin state. The polarizer and the analyzer were co-aligned so that the intensity of the transmitted neutron beam with no external magnetic fields was maximized. The polarization axes of the polarizer and the analyzer were along the Y-axis.

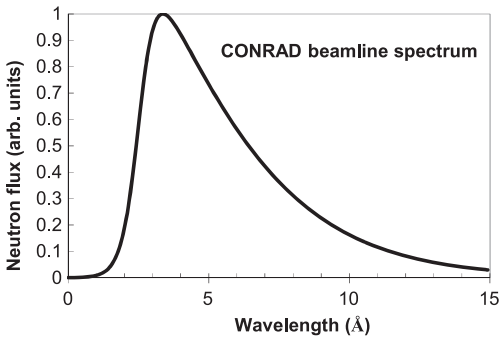

Figure 2. Spectrum of CONRAD beamline used in the polarized imaging experiments. No beam monochromatization was implemented.

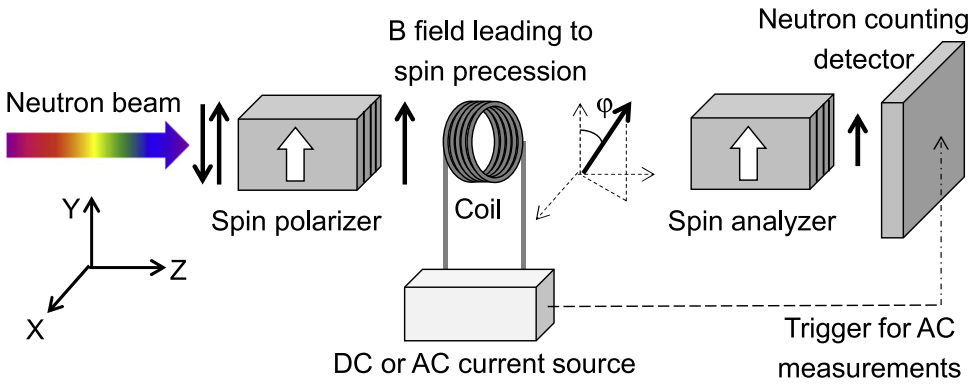

Figure 3. Schematic diagram of the experimental setup. A 5- or 15-loop coil installed between spin polarized and spin analyzer. Neutron counting detector is synchronized with the current source. Time and position of each neutron is detected. Polychromatic beam was used in experiment.

A neutron counting detector with microchannel plates, providing both position and time of neutron arrival was used in the experiments [21, 22, 27]. The active area of the detector was limited to 14×14 mm^2 and the spatial and temporal resolution was 55 μm and ~1 μs, respectively. High detection efficiency exceeding 50% for thermal and cold neutrons [28, 29] and was essential for the present studies of the dynamic magnetic fields where acquisition of many frames corresponding to various phases of the magnetic field variation was required. The detector was synchronized with the ac current source for the coil generating magnetic field with 3 kHz frequency. A coil with 5 and another coil with 15 loops of ~10 mm diameter were installed at a few cm distance from the analyzer, figure 3. A 1 mm aluminum wire coated by 0.1 mm insulation was used to form the coils shown in figure 4. The neutron attenuation of these coils was very low and thus the contrast in the images acquired in our experiments was determined almost exclusively by the spin precession in the magnetic field and not by the neutron attenuation by the sample. All the images reported in this paper were normalized by the 'open beam' images to eliminate the stripes from the structure of the polarizer and the analyzer, which consisted of multiple layers of the polarizing mirrors and Gd absorbers [25, 26].

For the static magnetic fields a dc current of 1–10 A was supplied to the coils and the resulting transmission images were accumulated by the detector over a 100 s period in most cases. The measurements of the dynamic magnetic field was performed simultaneously for all phases of the ac cycle, unlike a stroboscopic mode often used in time resolved neutron imaging experiments, when most of the neutrons are excluded from images by electronic shutter and only a short time range within each cycle is measured. In our experiments the time of each detected neutron was measured with sub-μs accuracy relative to the trigger synchronized to the ac current source. The events were binned online into a stack of images, each corresponding to a 2 μs wide period of the ac cycle, so that 166 phases of 3 kHz cycle were accumulated simultaneously, allowing an efficient data collection for a dynamic process with 333 μs period.

We used the full spectrum of the beam in order to increase the counting statistics for both dynamic and static experiments. As mentioned earlier, the presence of neutrons of various energies leads to a certain blurring of the magnetic field imaging as the rate of spin precession is proportional to neutron energy and more accurate future experiments will have to be conducted with somewhat monochromatized neutron beams (e.g. by a velocity

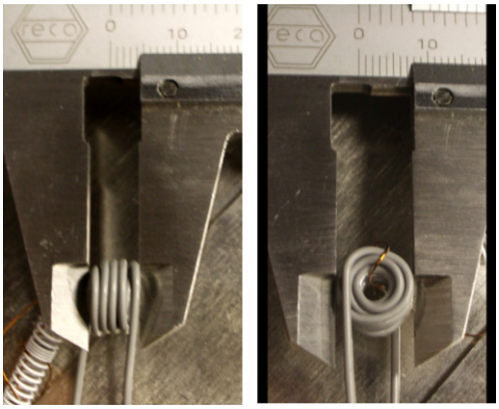

Figure 4. Photograph of 15-loop coil used for the polarized imaging experiments. Three layers of 5 loops were overlayed on top of each other to produce a larger magnetic field. The 5 loop coil was similar with only one 5-loop layer. The aluminium wire has very low neutron attenuation.

selector with its ~10% energy resolution or a double crystal monochromator with ~3% energy resolution). A pulsed neutron beam can also be used as the energies of neutrons can be recovered from their time of flight and thus images corresponding to different energies can be acquired simultaneously. The advantage of the pulsed neutron beam for polarization measurements is in the fact that a wide spectrum of energies can be used at the same time, thus allowing efficient quantification. Indeed the angle φ can be recovered explicitly from equation (5) without the bias of an undefined offset due to the modulus of the cosine [6, 24, 30].

3. Theoretical predictions of polarized neutron radiography of magnetic fields

All our experimental results of the corresponding measurements were compared to the calculated images for the 15 loop coil operating in dc and ac modes. The utilized calculation procedure of the resulting images can be applied to any magnetic field and is not limited to the field produced by our coil sample. To calculate the expected intensity distribution for a given sample we first compute the three-dimensional magnetic field $\vec{B}(x, y, z) = B_x(x, y, z),\ B_y(x, y, z),\ B_z(x, y, z)$ (in our case the field in a $20 \times 20 \times 30$ mm^3 volume around the coil, appendix A). Then for each position (x, y) the integrated angle of neutron precession as it propagates through the magnetic field is calculated numerically from equation (4) for the neutrons of various wavelengths λ. The details of integration of equation (4) are described in appendix B. Once the angle φ was found for the neutron arriving at the analyzer position the intensity of the neutron flux at position (x, y) is calculated from equation (5) assuming there is no attenuation of the neutron beam by absorption (low absorbing aluminum wire in our experiments). The image otherwise is modified by the attenuation of the sample if required, or results are correlated to attenuation corrected images through normalization. The calculation is repeated for each pixel (x, y) of the detector active area and the resulting transmission image $I(x, y)$ is calculated for a given current I in the coil and given neutron wavelength λ. Finally, to simulate the experiment at CONRAD beamline with a wide neutron spectrum multiple images are calculated for various neutron wavelengths (for the same magnetic field value) and those images are combined with weighted coefficients corresponding to the beam spectrum shown in figure 2.

4. Results

4.1. Dc magnetic fields

Initially we have measured the spin-polarized neutron images of static magnetic fields produced by 1–10 A dc currents in the 5 loop and 15 loop coils, figures 5 and 6. The observed fringing from the 5-loop coil indicates that even at 10 A the number of full 2π precessions of the spin in the XY-plane is small, while for the 15 loop coil 10 A create a magnetic field strong enough to produce multiple fringes in the resulting images. Some of those fringes cannot be resolved because of the use of the polychromatic neutron beam, image blurring by the beam divergence and the short period between the fringes at positions with maximum field values. The agreement between the calculated (figure 7) and measured polarized images confirms the validity of our modeling, which can be used for the pre-experimental analysis in future studies for the estimation of which magnetic fields can be resolved by our technique and what is the requirement for the beam monochromatization. The measured

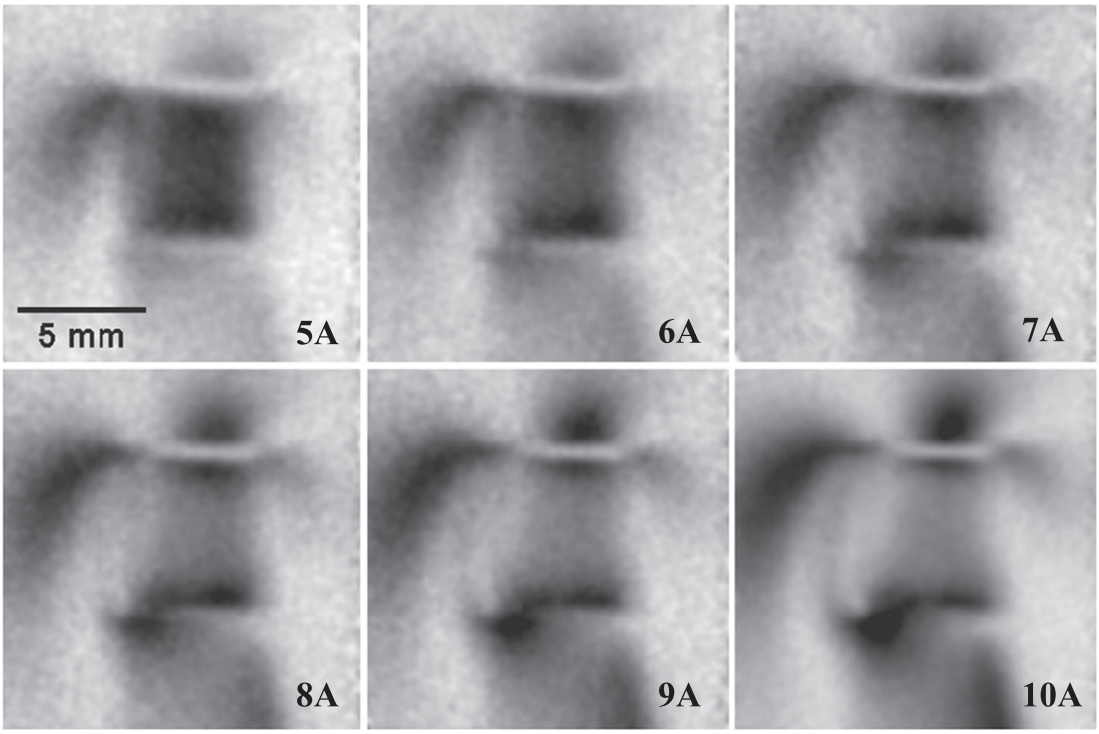

Figure 5. Spin-polarized neutron radiographs of a dc magnetic field produced by a 5-loop coil. The value of the dc current in the coil varied from 5 to 10 A, leading to increased neutron spin precession and resulting in more fringes seen in the images at a higher magnetic field.

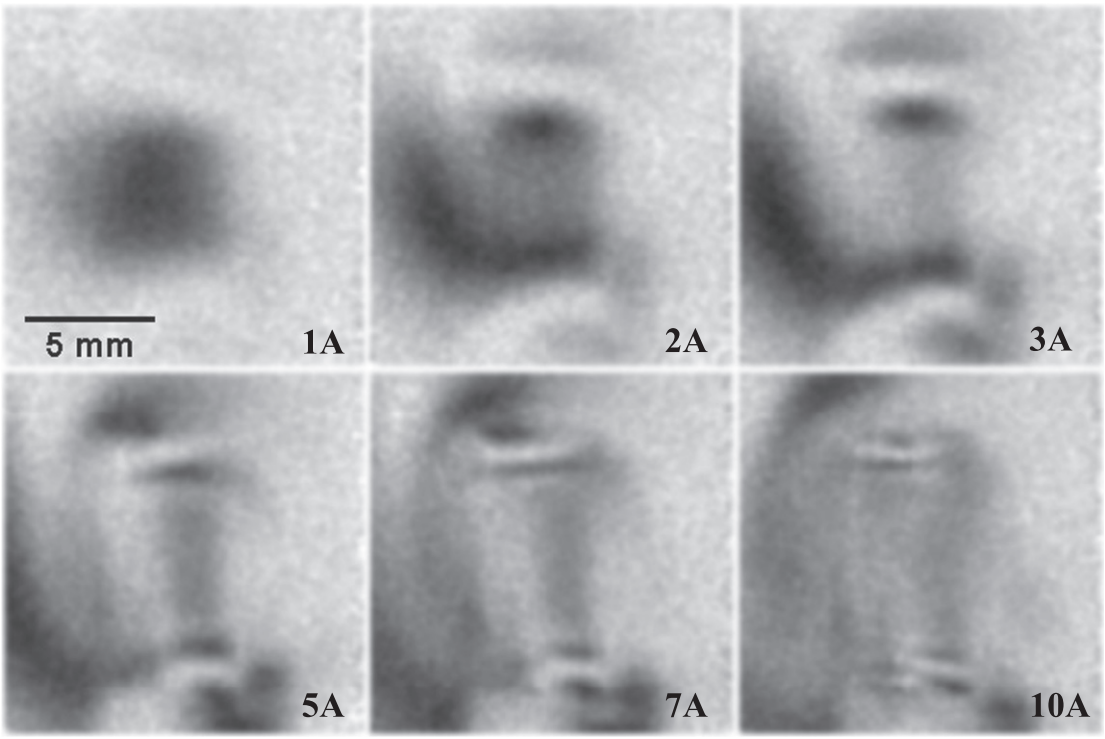

Figure 6. Spin-polarized neutron radiographs of a dc magnetic field produced by a 15-loop coil. The value of the dc current in the coil varied from 1 to 10 A.

magnetic fields produced by opposite currents, figure 8, also agree quite well with the results of our corresponding calculations, figure 9, although the asymmetry of the coil lead wires results in some asymmetry of the polarized images.

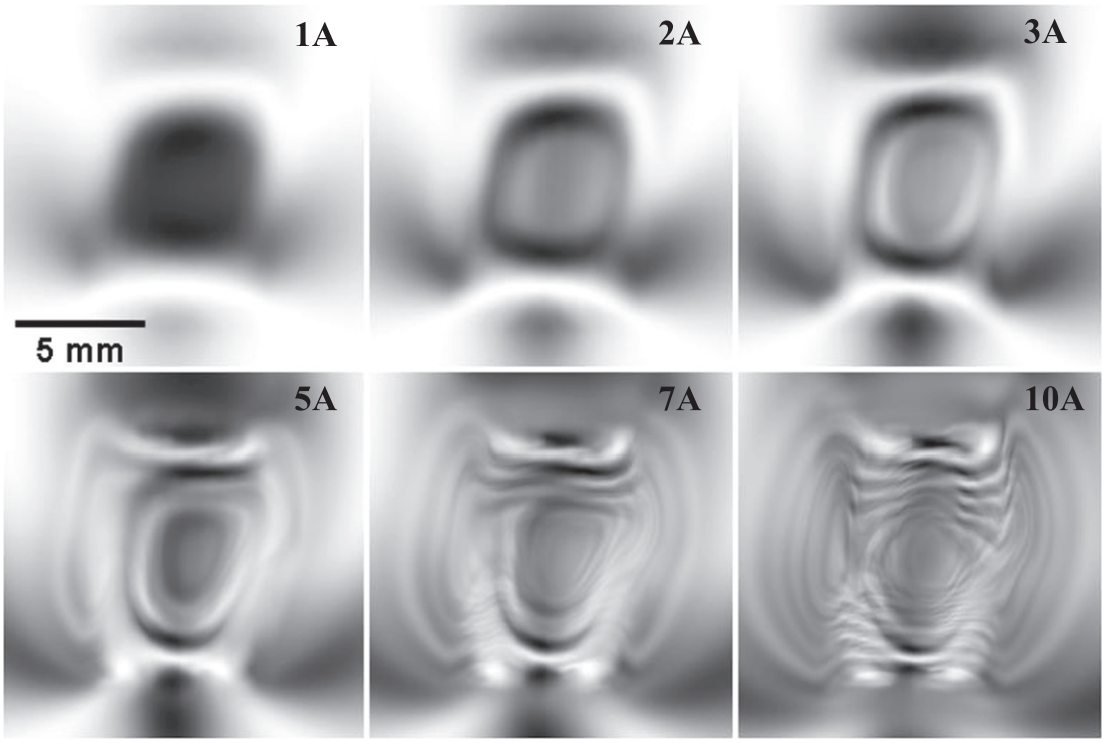

Figure 7. Simulated radiographs of a dc magnetic field produced by a 15-loop coil. The value of the dc current in the coil varied from 1 to 10 A. The images are calculated for the CONRAD beam spectrum shown in figure 2.

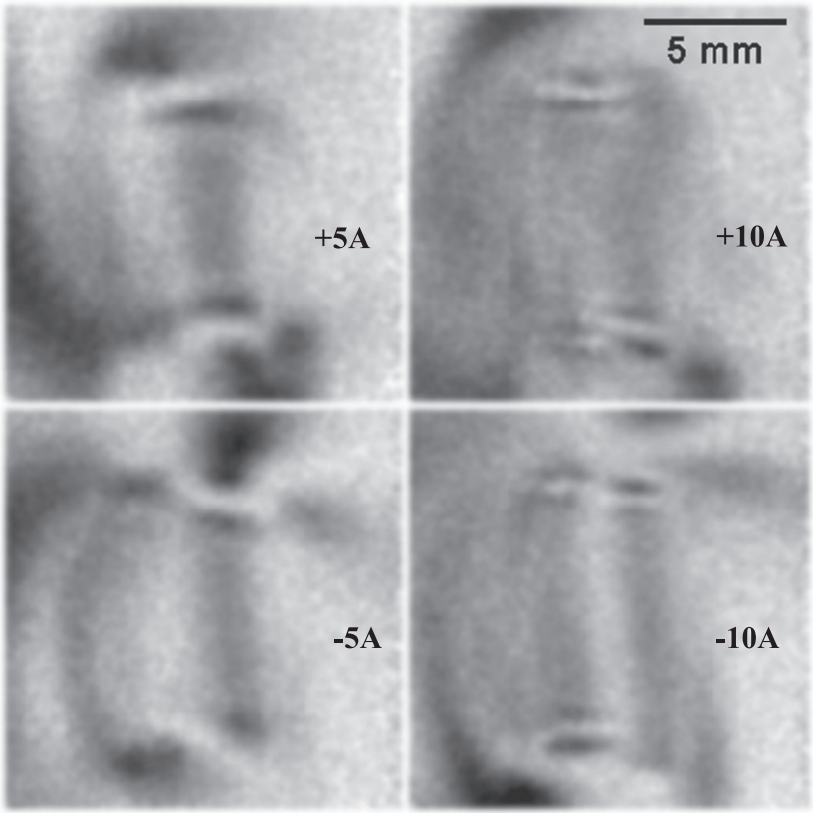

Figure 8. Spin-polarized neutron radiographs of a dc magnetic field produced by a 15-loop coil. Positive and negative 5 and 10 A currents are imaged, demonstrating the asymmetry of the magnetic field produced by the coil due to the geometry of the leads on the coil.

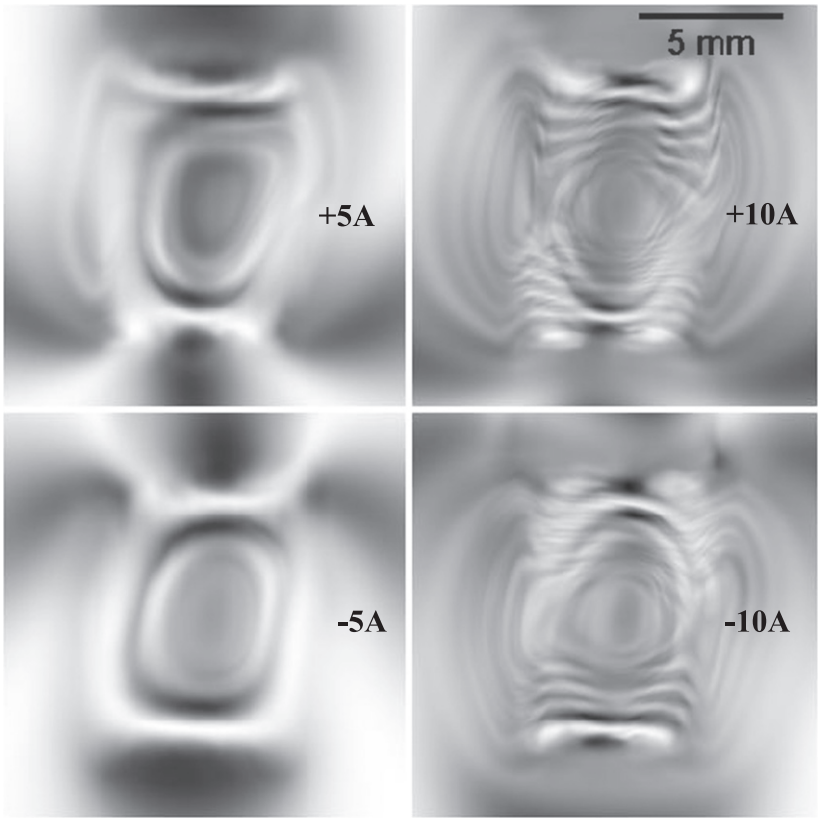

Figure 9. Simulated spin-polarized neutron radiographs of a dc magnetic field produced by a 15-loop coil. Positive and negative 5 and 10 A currents are calculated for the CONRAD beamline spectrum shown in figure 2.

4.2. Time-varying periodic magnetic fields

Imaging of dynamic magnetic fields in general is difficult as the polarized neutron fluxes are relatively low (10^5–10^7 n cm^{-2} s^{-1}) and a short exposure time (microseconds to milliseconds) is not sufficient to form an image with acceptable statistics. However, if the magnetic field varies periodically the neutron statistics can be improved by the integration of polarized neutron images at the same phase over multiple cycles. Stroboscopic imaging is one of the options where only a particular phase of the dynamic process is imaged by gating a fast imaging detector (e.g. scintillator screen coupled to a gated image intensifier followed by a CCD or CMOS readout). However, this approach has a serious limitation: the timing resolution of such experiments is fixed by the acquisition shutter and cannot be changed by the later analysis. Even worse, a large fraction of neutrons is not used for the imaging and multiple acquisitions have to be performed in order to cover the full cycle of the process, which is highly inefficient. Another approach is to use a neutron counting detector, which can provide both position and time resolution for each detected neutron. Synchronization of timing in such experiment to the dynamic process under study enables quasi-simultaneous detection of multiple phases of the cycle and flexible time binning. In that case only one measurement is required and the resulting time-resolved images are integrated over multiple cycles. In our dynamic experiments a neutron counting detector with Timepix readout was used to image a dynamic magnetic field produced by the 15-loop coil conducting a 3 kHz ac current. The detector and the coil were the same as in static measurements, only the current was changed from dc to ac. In the resulting data set the 333 μs wide cycle was split into 166 images each corresponding to a specific 2 μs wide phase of the process. The flexibility of this acquisition mode allowed subsequent grouping of the images into 10 μs wide slices (with the phase of each slice shown in figure 10). The measured neutron polarized images for the 2 A rms ac current are shown in figure 11 and for 10 A rms current in figure 12. A better visualization of the measured magnetic field dynamics can be found in the animation of the acquired images in the online supplemental materials[7]. The neutron statistics of dynamic images is lower than in dc current experiments as the process was split into 166 individual frames and a lower number of neutrons were acquired in each 55 μm pixel of our detector per acquisition frame compared to the static measurement. The simulated images corresponding to a 10 A rms current shown in figure 13 were calculated for the polychromatic beam spectrum of CONRAD beamline and

[7] The dynamic magnetic fields measured for a 3 kHz AC current in a coil imaged at CONRAD beamline facility as well as simulated images for the same coils are presented in the online supplemental material to this article (stacks.iop.org/NJP/17/043047/mmedia).

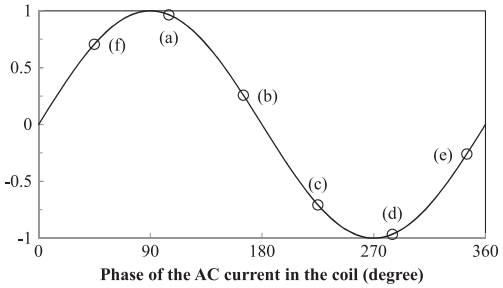

Figure 10. The phases of the magnetic field shown in figures 11–13. Neutrons of 10 μs time ranges (3% of magnetic field period) are grouped together to form the individual images of figures 11–13.

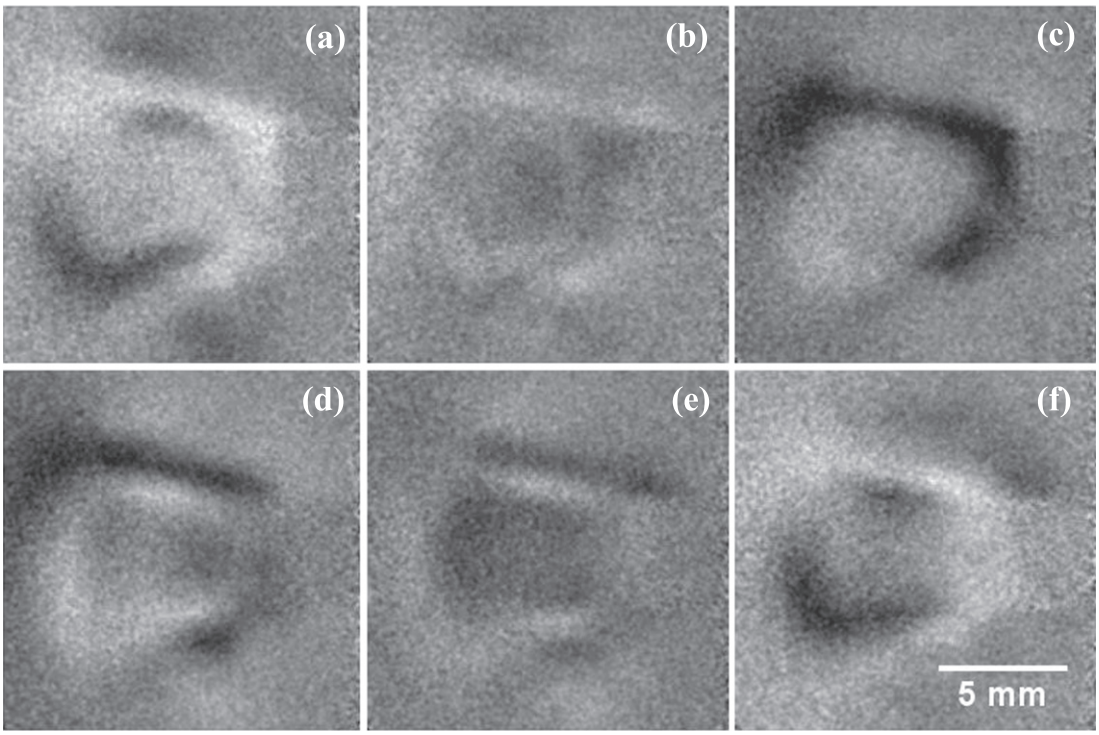

Figure 11. Spin-polarized neutron radiographs measured for different phases of a dynamic magnetic field. The field is produced by a 15-loop coil with a 3 kHz ac current with 2 A peak-to-peak amplitude. Each image here represents a 10 μs wide time slice of the ac cycle. The corresponding phases of the 3 kHz cycle are shown in figure 10. Multiple cycles of the process were imaged and grouped together to provide adequate statistics. All phases of the dynamic magnetic field are imaged quasi-simultaneously, which is enabled by the time tagging of each detected neutron relative to the phase of the ac current.

demonstrate the blurring of the fringes through the superposition of images corresponding to various neutron wavelengths. A detailed analysis of the wavelength dependence of such dynamic polarized neutron imaging is described in the next section.

5. Wavelength dependence of polarized neutron imaging

As seen from equation (4) the neutron spin precession angle depends both on the value of the magnetic field and the wavelength of the neutrons. In the experiments with a static magnetic field the contrast in the measured images is determined by the variation of the magnetic field across the field of view and by the monochromaticity of the beam. With a neutron beam of a relatively narrow energy range (e.g. formed by a double crystal monochromator at a continuous source) the magnetic field variation is represented by the oscillation of intensity across the image. Measurements with a pulsed neutron beam allow simultaneous detection of multiple energies and flexible energy binning improving the statistics and enabling more accurate quantification of the magnetic field values. However, in dynamic magnetic field measurements there is another factor affecting the

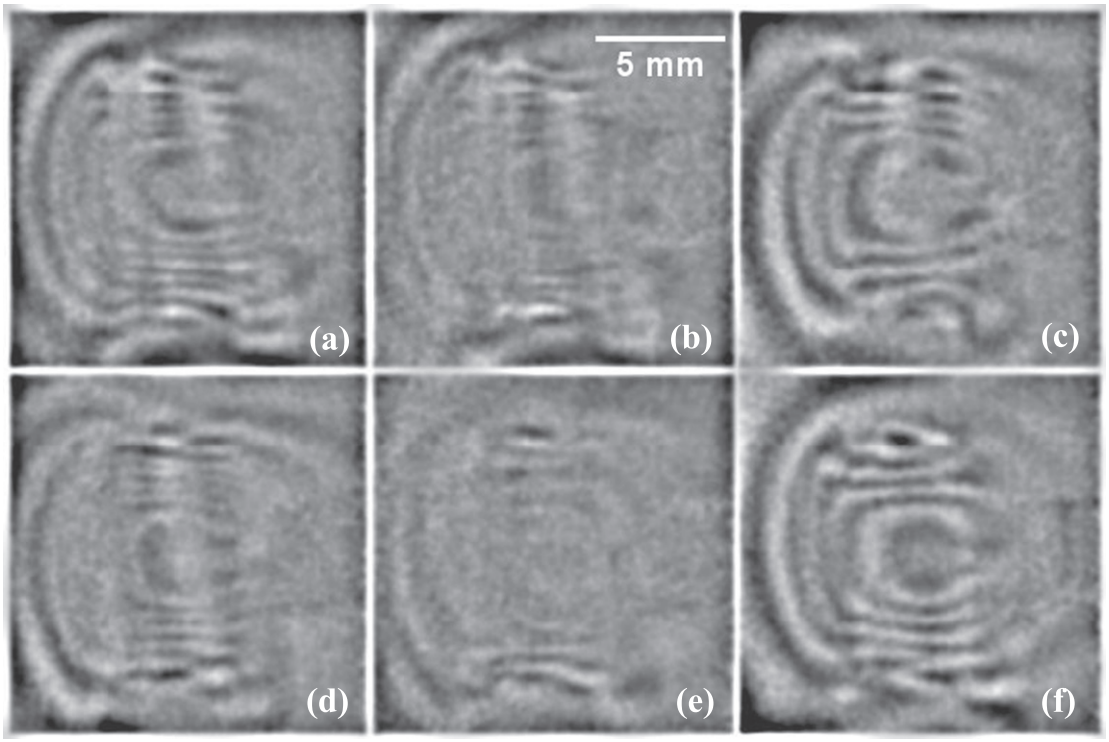

Figure 12. Same as figure 11 except for the ac current of 10 A rms. Compared to the figure 11 a larger number of fringes is detected in the images for the same phases of the 3 kHz cycle.

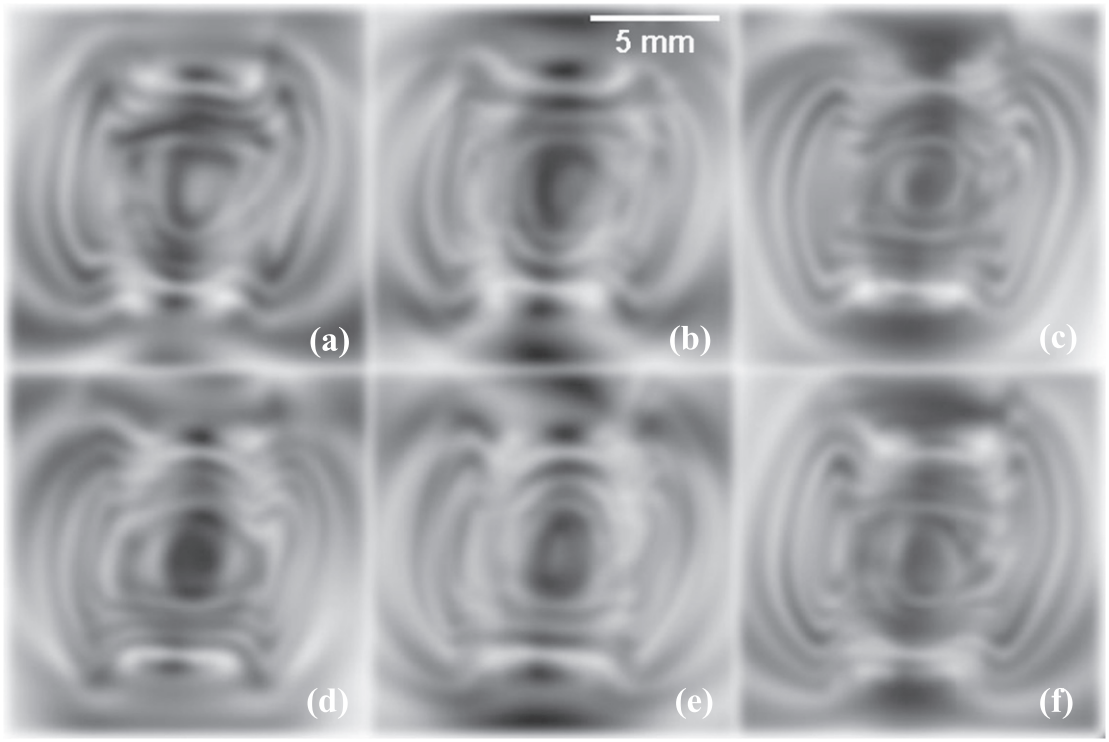

Figure 13. Simulated spin-polarized neutron radiographs for the experimental data shown in figure 12. Images of individual 10 μs wide time slices (3% of total cycle period) are calculated for the CONRAD beamline spectrum. The magnetic field is produced by a 15-loop coil running a 3 kHz current with the 10 A rms amplitude. 200 μm Gaussian blur is applied to the calculated images in order to simulate the experimental conditions where beam divergence in the ~170 mm gap between the sample and the detector led to image blurring.

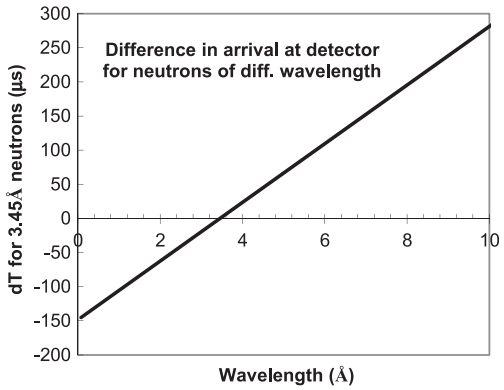

Figure 14. The time difference of neutron arrival at the detector for neutrons which were at the same location within the coil at the same time. Distance to the detector active area ~170 mm. Different phases of the ac field are imaged at the detection plane by neutrons of different energy.

contrast of the measured images and thus complicating the data analysis: neutrons of different wavelengths impinging on the detector at the very same time have experienced the magnetic field at different times and hence represent different phases of the dynamic magnetic field. Neutrons of various energies travel at different speeds through the gap between the sample and the detector. That leads to the fact that faster neutrons which interacted with a given phase of the magnetic field arrive at the detector earlier, simultaneously with colder neutrons which interacted with a different phase of the magnetic field. Thus two blurring effects on fringes occur in the dynamic imaging with polarized neutrons due to limited wavelength resolution: the first is due to the increase of the spin precession with neutron wavelength; the second is due to the fact that slower neutrons corresponding to a particular phase of the dynamic process arrive at the detector plane with some delay compared to the faster neutrons. Figure 14 demonstrates the time difference of the corresponding neutron arrival for various wavelengths. Here the time of arrival of neutrons corresponding to the same phase of the dynamic process is calculated for neutrons of various energies, assuming that neutrons of 3.45 Å arrive at time t = 0. The difference in arrival time between 1 and 6 Å neutrons is ~200 μs for the 170 mm distance between the coil and the detector used in our experiment. That implies that there is about ~1–2 μs un-sharpness for 1% wavelength resolution in that energy range. To demonstrate the extent of this dynamic blurring by the polychromatic neutron beam we have calculated the images corresponding to the same phases of ac cycle in the coil as shown in figure 13 for the neutrons of three different wavelengths, figures 15–17. For 2.025 Å neutrons the minimum number of fringes is observed at the phase corresponding to the phase marked as (a) in figure 10, while it is close to the phase (b) for 3.45 Å neutrons and phase (c) for neutrons of 4.875 Å wavelength. Therefore if a wide spectrum neutron beam is used for imaging of dynamic magnetic fields multiple phases of the dynamic field overlap in the resulting images. Consequently, at a continuous source a compromise needs to be found between the reduced neutron statistics and the degree of beam monochromatization. The possibility to image with intrinsic energy resolution over a broad wavelength band at a pulsed neutron source is probably the best option for imaging the dynamic magnetic fields as it also provides the basis for accurate data analysis. However, since the frequency of neutron sources is fixed to a certain value and the frequency of the dynamic process of interest can be different, for each neutron pulse the dynamic process will be probed by a random correlation of process phase and neutron energy. With multiple neutron pulses acquired, all phases can be imaged at all neutron energies available in a particular beam. However, care has to be taken to avoid some harmonics between the two frequencies involved. Analyses of the probed magnetic field can then be performed wavelength by wavelength. These results can subsequently be combined for the accurate quantification of the magnetic field values without the need for the absolute field calibration required for a single monochromatic measurement.

To demonstrate the potential of quantitative analysis of magnetic fields measured at a pulsed neutron beamline we simulated the data set which could be obtained in such experiment with the same 15-loop coil sample as in our continuous source experiment. A static magnetic field is simulated in that case, although similar methods will be applicable for the dynamic studies, where each phase is analyzed separately in the same way as in case of a corresponding static field. At a pulsed source a set of images, each measured with a certain neutron energy can be acquired. Thus the energy dependence of the measured intensity is obtained for each pixel of the resulting data set. In the simplest case, when the magnetic field distribution has only one component, which is perpendicular to the initial beam polarization vector, the spin precession has a sinusoidal dependence on the neutron wavelength as seen from equations (4) and (5). The period of that fluctuation can be used to calculate the value of the measured magnetic field. As mentioned earlier, this field quantification technique does not

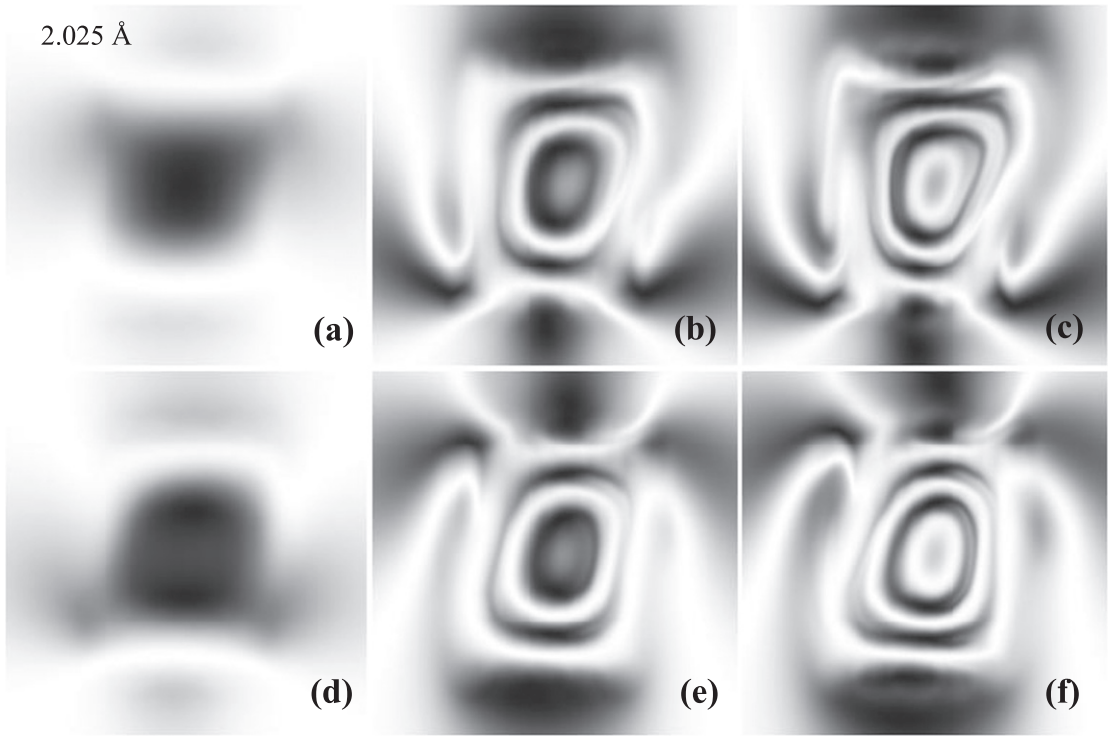

Figure 15. Simulated spin-polarized neutron radiographs of a 3 kHz magnetic field produced by a 15-loop coil with 10 A rms ac current. A monochromatic neutron beam of 2.025 Å wavelength is assumed in the calculations. The phases of the 3 kHz cycle are shown in figure 10. The distance to the detector is 170 mm.

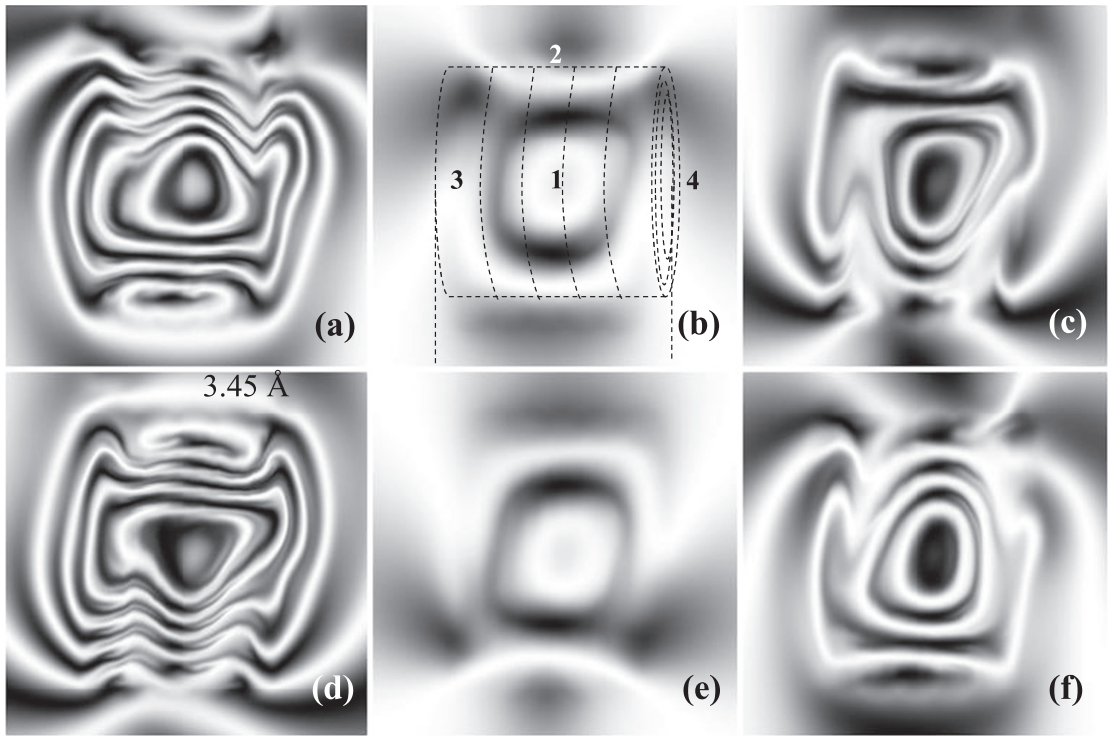

Figure 16. Same as figure 15 except calculated for neutrons of 3.45 Å wavelength. Note that minimum field is measured by the detector at times close to phases (b) and (e) of figure 10, while the 2.025 Å neutrons arriving earlier to the detector show the minimum field close to phases (a) and (d). Thus images corresponding to significantly different phases of the magnetic field overlap at the detector plane. Hence, a beam with relatively narrow spectrum needs to be used to measure dynamic magnetic fields accurately. More fringes are also seen for the longer wavelength neutrons due to the fact that these neutrons spend more time moving through the magnetic field. The numbers in image (b) indicate the areas where the neutron transmission spectra of figure 18 were obtained.

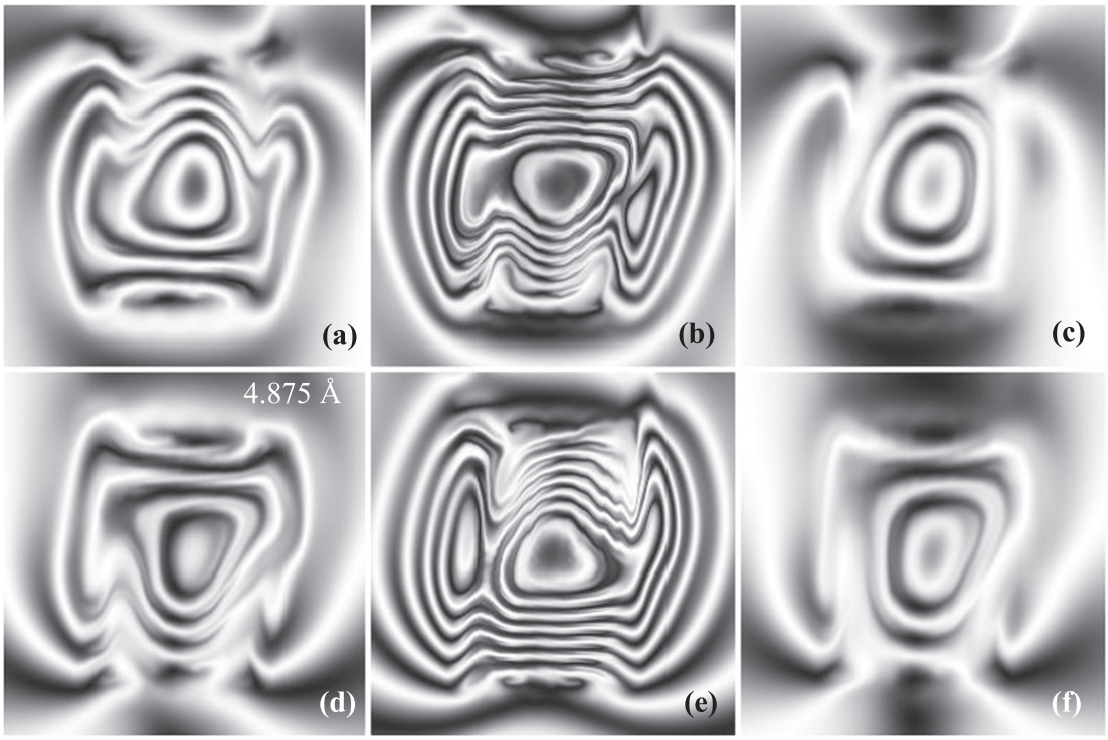

Figure 17. Same as figure 15 except calculated for neutrons of 4.875 Å wavelength. Note that minimum field is measured by the detector at times close to phases (c) and (f) of figure 10.

require counting of fringes from the zero-field area and provides the field value for a given pixel of the image. However, in a general experiment with a three-dimensional magnetic field distribution the precession of neutron spin is more complicated and a more detailed analysis has to be performed with measurements of different orientation of spin analyzer and polarizer. Figure 18 demonstrates the calculated intensity variation with neutron wavelengths for several areas in and around the coil for 5 and 10 A dc currents. In the center of the coil (area 1 of figure 16(b)), where the magnetic field is predominantly directed along the *X*-axis, the spin precession occurs mostly in the *XY*-plane resulting in a nearly sinusoidal variation of the measured neutron intensity in that area. Same is valid in area 2, where the field is not as strong as in area 1, the variation of intensity is with a larger period with respect to the neutron wavelength. However, in areas 3 and 4, the presence of considerable magnetic field components in the *YZ*- and *XZ*-planes results in a complicated pattern. To reconstruct the three-dimensional magnetic field distribution quantitatively more measurements are required, as explained earlier. However, the field pattern can still be somewhat visualized in a single measurement, as seen in simulated images in figures 15–17.

6. Summary and conclusion

The remote imaging of static magnetic fields demonstrated in previous studies [5–10], has been extended in this paper to time-varying periodic fields, which provides a powerful new tool for dynamic applications where probing the magnetic field can otherwise be difficult if not impossible. The ability of neutrons to penetrate some materials (e.g., metals) and at the same time to provide quantified information on the distribution of the magnetic field within (or even behind) these materials, enables unique studies to be carried out—for example, the realignment of magnetic domains under the influence of external magnetic fields, measurement of the magnetic fields within complicated structures, and so on. It is shown that careful planning of the experimental setup is required for accurate quantification of the magnetic field distribution. In particular, a compromise between the image statistics (or integration time) and beam monochromatization—factors which determine the accuracy of the reconstructed distribution—must be found for any specific experiment at a continuous source. Selection of a particular neutron energy range is required for the measurement of a given range of magnetic field values, because the spatial resolution of polarized neutron imaging sets the limits on the distance between the fringes which are still resolvable. Thus stronger magnetic fields may be better imaged with neutrons having shorter wavelengths, while weaker magnetic fields require imaging with longer wavelengths. The limits of the

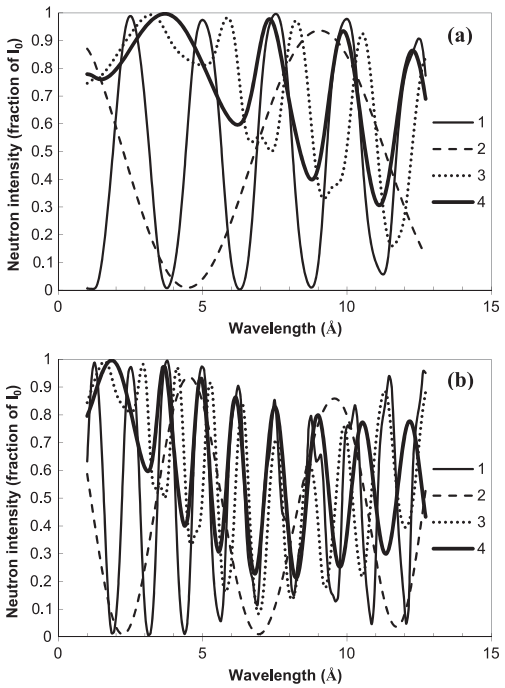

Figure 18. Neutron transmission spectra calculated for a 15-loop coil for the areas shown in figure 16(b). (a) For a 5 A dc current. (b) 10 A dc current. The nearly sinusoidal variation of measured neutron intensity is observed in the middle and above the coil (areas 1 and 2), where the field is predominantly perpendicular to the neutron spin polarization. There the spin precession is almost exclusively in the *XY* plane. However, in areas 3 and 4 the presence of the magnetic field fringes leads to a three-dimensional precession of the neutron spin, resulting in a deviation of transmission spectra from a purely sinusoidal curve.

quantification of spin precession are defined by the minimum distance between the fringes which can still be resolved by a particular experimental setup. In that respect, providing a more compact analyzer device will be very helpful, allowing reduction in the distance between the sample and the detector area, thus reducing image blurring due to the neutron beam divergence. In principle, spatial resolutions down to ~10 μm can be achieved using the latest high resolution neutron imaging detectors [27, 31]. Thus fringes as close as 20 μm can be resolved, provided adequate neutron statistics can be achieved and the image blurring remains below 10 μm.

The limit on the frequency of periodically changing magnetic fields in neutron imaging experiments is determined by the energy resolution of the beam ($\Delta E/E$) and the timing resolution of current neutron imaging detectors—which can be of the order of sub-microsecond [21–23]. The limited energy resolution can cause overlap of adjacent phases of a dynamic process due to the fact that neutrons have different travel times between sample and detector, including the finite length of the spin analyzer. Faster neutrons representing a particular phase of the *B* field will arrive at the detector simultaneously with slower neutrons representing a preceding phase of the *B* field, and that will constrain the frequency of the dynamic process, which can be studied at a particular beam facility. At a reactor source, the energy resolution is usually defined by the mosaicity of the double crystal monochromator being used, leading typically to resolutions of $\Delta E/E \sim 3\%$—a compromise between the neutron flux and energy resolution. At pulsed sources, energy resolution is limited by the width of the neutron pulse, typically 10–100 μs for thermal and cold neutrons at short pulse sources. Therefore, processes as fast as 100 kHz can still be studied with the present reactor-based and pulsed experimental facilities, using compact spin analyzers which minimize the distance between the sample and the detector.

The potential to quasi-simultaneously measure images at multiple energies makes pulsed sources very attractive for imaging of magnetic fields with an expanded dynamic range. However, accurate quantitative reconstruction algorithms still need to be established, especially for three-dimensional reconstruction problems. Current developments at pulsed neutron sources [24] are very promising, and represent a significant addition to methods already being used at continuous neutron sources.

Moreover, simulation and modeling of images for a specific experimental setup and magnetic field distribution should prove very beneficial for the optimization of a particular experiment, especially taking into account relatively long integration times required for accurate quantification with accompanying high spatial resolution.

Acknowledgments

The authors would like to acknowledge the generous donation of Vertex FPGAs and ISE design suite by Xilinx Inc. of San Jose, California through their Xilinx University Program. The detector used in these experiments was developed within the Medipix collaboration. This work was supported in part by the U.S. Department of Energy under STTR Grants No. DE-FG02-07ER86322, DE-FG02-08ER86353 and DE-SC0009657.

Appendix A. Calculation of the magnetic field distribution around folded 15-loop coil with lead wires

To calculate the neutron spin precession in a magnetic field generated by the solenoid coil used in our experiments the three-dimensional distribution of the magnetic field first needs to be determined. The coil formed by a 1 mm aluminum wire with 15 loops folded by stacked 5 loop layers had two lead wires, as shown in figure 3 and figure 16(b). The magnetic field in each point around the coil was calculated from the Biot–Savart law

$$d\vec{B}(x,y,z)=\begin{cases}\dfrac{\mu_0 I}{4\pi}\dfrac{d\vec{w}\times\vec{r}(x,y,z)}{|\vec{r}|^3};\ |\vec{r}|\geqslant\dfrac{d}{2}\\ \dfrac{\mu_0 I}{4\pi}\dfrac{d\vec{w}\times\vec{r}(x,y,z)}{\left(\frac{d}{2}\right)^3};\ |\vec{r}|<\dfrac{d}{2}\end{cases}, \tag{A1}$$

$$d\vec{w}\times\vec{r}(x,y,z)=\begin{vmatrix} i & j & k\\ dw_x & dw_y & dw_z\\ r_x & r_y & r_z\end{vmatrix}, \tag{A2}$$

where I is the current in the coil, $d\vec{w}$ is the small section of the wire and $\vec{r}(x,y,z)$ is the vector from the section of the wire to point (x,y,z) where the magnetic field is calculated. The coil in our calculations was split into five sections: three overlapping 5-loop sections and two lead wires. The diameters of the three overlapping 5-loop sections were 9.3, 6.9 and 4.5 mm. The lead wire N1 was connected to the external loops with diameter 9.3 mm, and the wire N2 was connected to the internal loops with diameter 4.5 mm, making the coil and the resulting magnetic field asymmetric. The integration of equation (A1) over the coil loops is performed according to equations (A3) and (A4):

$$dw_x=\begin{cases}\dfrac{dw}{\sqrt{1+\frac{d^2}{P^2}}};\ I>0\\ -\dfrac{dw}{\sqrt{1+\frac{d^2}{P^2}}};\ I<0\end{cases};\quad dw_y=\frac{\cos\left(\frac{2w}{d}\right)dw}{\sqrt{1+\frac{P^2}{d^2}}};\ dw_z=\frac{\sin\left(\frac{2w}{d}\right)dw}{\sqrt{1+\frac{P^2}{d^2}}}; \tag{A3}$$

$$r_x=x-\left(x_0+\frac{P}{d}w\right);\ r_y=y-\frac{d}{2}\sin\frac{2w}{d};\ r_z=z-\frac{d}{2}\cos\frac{2w}{d}; \tag{A4}$$

where x_0 is the position of the left edge of the coil, P is the period of the coil along X-axis (width of the coil divided by the number of loops in one layer) and d is the diameter of a particular coil layer. The final field $\vec{B}$ was calculated for each point (x,y,z) in a $2\times2\times2$ cm^3 volume enclosing the coil from the superposition of the fields from the three layers (5 loops each, middle layer has the current in opposite direction along X-axis compared to the outer and inner loops) and two lead wires.

Figures 19 and 20 show the calculated distribution of magnetic field produced by our 15-loop coil conducting a 10 A dc current. The values of the magnetic field components averaged over a 3 cm path along Z-axis of our coil are within few millitesla range, with the maximum field values along X-axis, reaching ~20 mT at the center of the coil.

Appendix B. Integration of neutron spin precession

The calculation of the spin precession in a magnetic field is performed along the neutron propagation path, which is split into small steps. Integration of spin precession in three-dimensional space is performed on each step. The precession of vector $\vec{S}(l)$ around vector $\vec{B}(l)$ is calculated according to the following procedure.

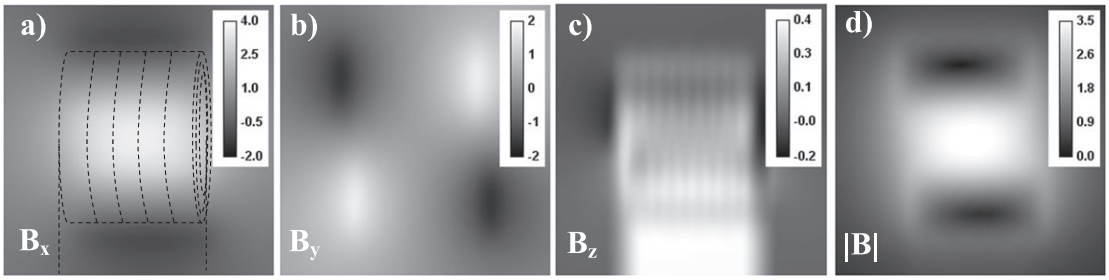

Figure 19. Calculated values of the magnetic field generated by a 15 loop coil with 10 A dc current. *The values are averaged over 3* cm *distance along Z-axis* (neutron propagation direction). (a), (b), (c)—*B*-field components along *X*, *Y* and *Z* axes, (d)—the module of the averaged magnetic field. The legend indicates the values of the magnetic field in mT. The coil orientation is shown by the dashed lines in (a).

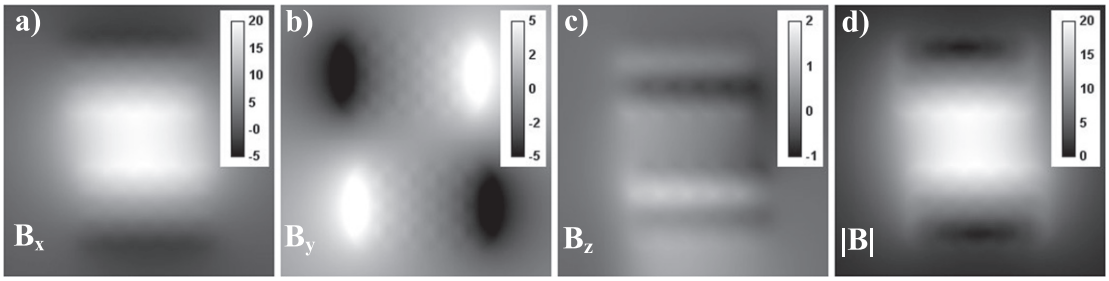

Figure 20. Same as figure 19, but calculated for a fixed position along *Z*-axis at the center of the coil. The legend indicates the values of the magnetic field in mT.

Initially the vector $\vec{B}\,(l)$ is aligned with axis Z'' by two rotations of the system of coordinates: first counterclockwise by the angle $\left(\frac{\pi}{2} - \varphi_B\right)$ around Y axis, figure 21(a)

$$\varphi_B = \begin{cases} \text{arctg}\dfrac{B_z}{B_x} + \dfrac{\pi}{2}\left(1 - \dfrac{B_x}{|B_x|}\right);\ \boldsymbol{B_x} \neq 0 \\ 0;\ B_z = 0 \\ \dfrac{\pi}{2}\dfrac{B_z}{|B_z|};\ \boldsymbol{B_z} \neq 0,\ \boldsymbol{B_x} = 0 \end{cases} \tag{B1}$$

and then clockwise by the angle $\left(\frac{\pi}{2} - \theta_B\right)$ around X' axis, figure 21(b).

$$\theta_B = \begin{cases} \arccos\dfrac{B_{y'}}{|\vec{B}|};\ |\vec{B}| \neq 0 \\ 0;\ |\vec{B}| = 0. \end{cases} \tag{B2}$$

After that the system of coordinates is rotated clockwise by the angle η to position the vector $\vec{S}\,(l)$ into $Y'''Z'''$ plane, figure 21(c)

$$\eta = \begin{cases} \text{arctg}\dfrac{S_{x''}}{S_{y''}} + \dfrac{\pi}{2}\left(1 - \dfrac{S_{y''}}{|S_{y''}|}\right);\ \boldsymbol{S_{x''}} \neq 0,\ \boldsymbol{S_{y''}} \neq 0 \\ 0;\ \boldsymbol{S_{x''}} = 0 \\ \dfrac{\pi}{2}\dfrac{S_{x''}}{|S_{x''}|};\ \boldsymbol{S_{x''}} \neq 0,\ \boldsymbol{S_{y''}} = 0. \end{cases} \tag{B3}$$

At that point the vector $\vec{S}\,(l)$ and $\vec{B}\,(l)$ are both in the plane $Y'''Z'''$ and the precession of vector $\vec{S}\,(l)$ can now be calculated from its rotation by an angle φ around Z''' axis (vector $\vec{B}\,(l)$) according to equation (3), figure 21(d) with sin α found from

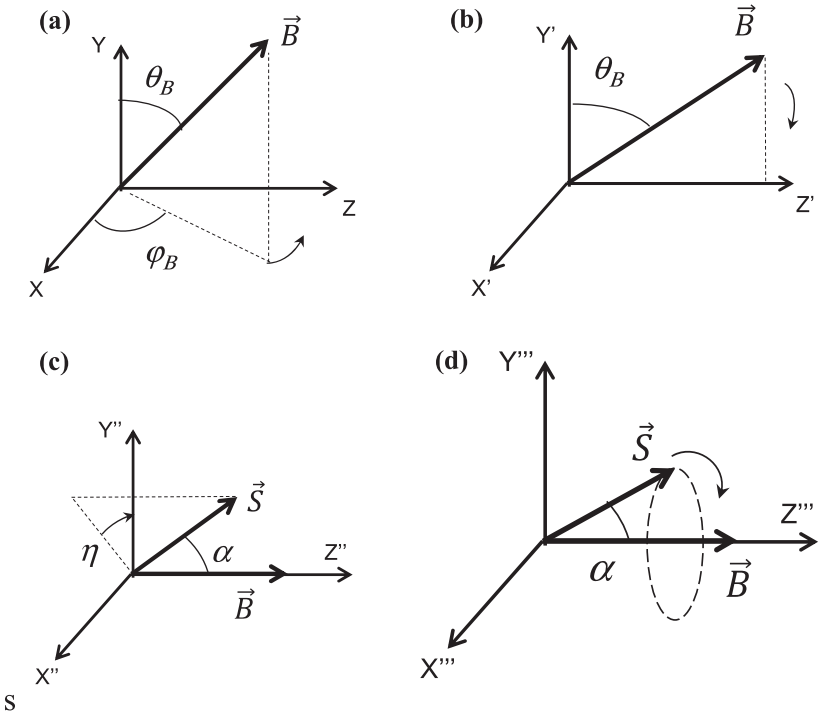

Figure 21. Calculation of neutron spin precession on each step of integration along neutron travel path. With three rotation of the system of coordinates both vectors $\vec{S}$ and $\vec{B}$ are brought into $Y'''Z'''$ plane and then vector $\vec{S}$ is precessed around $\vec{B}$ by an appropriate angle φ calculated from equation (3).

$$\sin\ \alpha = \frac{\left|Sy'''\right|}{\sqrt{S_{y'''^2} + S_{z'''^2}}} \tag{B4}$$

After that precession the system of coordinates $X'''Y'''Z'''$ is transferred back to XYZ by three inverse rotations by angles $-\eta, \left(\theta_B - \frac{\pi}{2}\right)$ and $\left(\varphi_B - \frac{\pi}{2}\right)$. That process is repeated along the neutron path between the polarizer and the analyzer in the presence of the magnetic field and the vector $\vec{S}\ (l)$ is obtained at the position of the analyzer entrance. The intensity of neutron flux in pixel (x, y) of the image was then calculated from equation (5) with the angle φ of the neutron spin in XY plane calculated from the equation

$$\cos\ \varphi = \begin{cases} \dfrac{S_y}{\sqrt{S_x^2 + S_y^2}};\ \sqrt{S_x^2 + S_y^2} \neq 0 \\ \dfrac{\pi}{2};\ \sqrt{S_x^2 + S_y^2} = 0. \end{cases} \tag{B5}$$

References

[1] Schlenker M *et al* 1980 Imaging of ferromagnetic domains by neutron interferometry *J. Magn. Magn. Mater.* **15-18** 1507–9
[2] Podurets K M, Petrenko A V, Somenkov V A and Shil'shtein S S 1994 Neutron radiography with depolarized contrast *Zh. Tekh. Fiz.* **67** 134–6
[3] Leeb H, Hochhold M, Badurek G, Buchelt R J and Schricker A 1998 Neutron magnetic tomography: a feasibility study *Aust. J. Phys.* **51** 401–13
[4] Strobl M, Treimer W, Keil S, Walter P and Manke I 2007 Magnetic field induced differential neutron phase contrast imaging *Appl. Phys. Lett.* **91** 254104
[5] Kardjilov N, Manke I, Strobl M, Hilger A, Treimer W, Meissner M, Kristi T and Banhart J 2008 Three-dimensional imaging of magnetic fields with polarized neutrons *Nat. Phys.* **4** 399–403
[6] Strobl M, Kardjilov N, Hilger A, Jericha E, Badurek G and Manke I 2009 Imaging with polarized neutrons *Physica* B **404** 2611–4
[7] Manke I, Kardjilov N, Strobl M, Hilger A and Banhart J 2008 Investigation of the skin effect in the bulk of electrical conductors with spin-polarized neutron radiography *J. Appl. Phys.* **104** 076109
[8] Dawson P M, Manke I, Kardjilov N, Hilger A, Strobl M and Banhart J 2009 Imaging with polarized neutrons *New J. Phys.* **11** 043013
[9] Schulz M, Neubauer A, Masalovich S, Mühlbauer M, Calzada E, Schillinger B, Pfleiderer C and Böni P 2010 Towards a tomographic reconstruction of neutron depolarization data *J. Phys.: Conf. Ser.* **211** 012025
[10] Treimer W 2014 Radiography and tomography with polarized neutrons *J. Magn. Magn. Mater.* **350** 188–98

[11] Grünzweig C et al 2010 Visualizing the propagation of volume magnetization in bulk ferromagnetic materials by neutron grating interferometry J. Appl. Phys. 107 09D308
[12] Manke I et al 2010 Three-dimensional imaging of magnetic domains Nat. Commun. 1 125
[13] Piegsa F M, van den Brandt B, Hautle P and Konter J A 2008 Neutron spin phase imaging Nucl. Instrum. Methods A 586 15–7
[14] Strobl M, Pappas C, Hilger A, Wellert S, Kardjilov N, Seidel S O and Manke I 2011 Polarized neutron imaging: a spin-echo approach Physica B 406 2415–8
[15] Kardjilov N et al 2011 Neutron tomography instrument CONRAD at HZB Nucl. Instrum. Methods A 651 47–52
[16] Calzada E, Schillinger B and Grunauer F 2005 Construction and assembly of the neutron radiography and tomography facility ANTARES at FRM II Nucl. Instrum. Methods A 542 38–44
[17] Kaestner A P, Hartmann S, Kühne G, Frei G, Grünzweig C, Josic L, Schmid F and Lehmann E H 2011 The ICON beamline—a facility for cold neutron imaging at SINQ Nucl. Instrum. Methods. A 659 387–93
[18] Santisteban J R, Daymond R, James J A and Edwards L 2006 ENGIN-X: a third-generation neutron strain scanner J. Appl. Cryst. 39 812–25
[19] Maekawa F et al 2009 NOBORU: J-PARC BL10 for facility diagnostics and its possible extension to innovative instruments Nucl. Instrum. Methods A 600 335–7
[20] Crow L, Robertson L, Bilheux H, Fleenor M, Iverson E, Tong X, Stoica D and Lee W T 2011 The CG1 instrument development test station at the high flux isotope reactor Nucl. Instrum. Methods A 634 S71–4
[21] Tremsin A S 2012 High resolution microchannel plates neutron counting detectors and their applications in neutron radiography, diffraction and resonance absorption imaging Neutron. News 23 35–8
[22] Tremsin A S, Vallerga J V, McPhate J B, Siegmund O H W and Raffanti R 2013 High resolution photon counting with MCP-timepix quad parallel readout operating at >1 kHz frame rates IEEE Trans. Nucl. Sci. 60 578–85
[23] Parker J D et al 2013 Spatial resolution of a μPIC-based μPIC-based neutron imaging detector Nucl. Instrum. Methods A 726 155–61
[24] Shinohara T et al 2011 Quantitative magnetic field imaging by polarized pulsed neutrons at J-PARC Nucl. Instrum. Methods A 651 121–5
[25] Krist T, Kennedy S J, Hick T J and Mezei F 1998 New compact neutron polarizer Physica B 241–243 82–5
[26] Krist T, Peters J, Shimizu H M, Suzuki J and Oku T 2005 Transmission bender for polarizing neutrons Physica B 356 197–200
[27] Tremsin A S, McPhate J B, Vallerga J V, Siegmund O H W, Feller W B, Lehmann E, Kaestner A, Boillat P, Panzner T and Filges U 2012 Neutron radiography with sub-15 μm resolution through event centroiding Nucl. Instrum. Methods A 688 32–40
[28] Tremsin A S, Feller W B and Downing R G 2005 Efficiency optimization of neutron imaging detectors with 10B doped MCPs Nucl. Instrum. Methods A 539/1-2 278–311
[29] Tremsin A S, McPhate J B, Vallerga J V, Siegmund O H W, Feller W B and Lehmann E 2011 Improved efficiency of high resolution thermal and cold neutron imaging Nucl. Instrum. Methods . A 628 415–8
[30] Strobl M 2009 Future prospects of imaging at spallation neutron sources Nucl. Instrum. Methods A 604 646–52
[31] Williams S H, Hilger A, Kardjilov N, Manke I, Strobl M, Douissard P A, Martin T, Riesemeier H and Banhart J 2012 Detection system for microimaging with neutrons J. Instrum. 7 P02014–02014